Coevolution-guided mapping of the Type VI secretion membrane complexbaseplate interface

Etienne Vanlioğlu, Yoann Santin, Isaac Filella-Merce, Riccardo Pellarin, Eric Cascales

Coevolution-guided mapping of the Type VI secretion membrane complex-baseplate interface.

Etienne Vanlioğlu[1,¶], Yoann G. Santin[1,‡], Isaac Filella-Merce[2,†], Riccardo Pellarin[2], and Eric Cascales[1,*]

Running head: T6SS baseplate-membrane complex interaction.

[1] Laboratoire d'Ingénierie des Systèmes Macromoléculaires (LISM), Institut de Microbiologie, Bioénergies et Biotechnologie (IM2B), CNRS – Aix-Marseille Université UMR7255, 31 Chemin Joseph Aiguier CS70071, 13402 Marseille Cedex 20, France.

[2] Structural Bioinformatics Unit, Department of Structural Biology and Chemistry, Institut Pasteur, CNRS UMR 3528, 28 rue du Docteur Roux, 75015 Paris, France

* Correspondence to Eric Cascales: Institut de Microbiologie, Bioénergies et Biotechnologie (IM2B), CNRS – Aix-Marseille Université, Marseille, France. cascales@imm.cnrs.fr (E.C.)

[¶] Current address: ImChecks Therapeutics, 31 Chemin Joseph Aiguier CS70071, 13402 Marseille Cedex 20, France

[‡] Current address: De Duve Institute, Bacterial Cell Biology, Université Libre de Bruxelles, Avenue Hippocrate 75, 1200 Brussels, Belgium

[†] Current address: Barcelona Supercomputing Center, Plaça d'Eusebi Güell, 1-3, 08034, Barcelone Spain

Characters count (including spaces): 48,000
Table: 1
Figures: 6
Supplemental material: 1 Table, 2 Figures

ABSTRACT

The type VI secretion system (T6SS) is a multiprotein weapon evolved by Gram-negative bacteria to deliver effectors into eukaryotic cells or bacterial rivals. The T6SS uses a contractile mechanism to propel an effector-loaded needle into its target. The contractile tail is built on an assembly platform, the baseplate, which is anchored to a membrane complex. Baseplate-membrane complex interactions are mainly mediated by contacts between the C-terminal domain of the TssK baseplate component and the cytoplasmic domain of the TssL inner membrane protein. Currently, the structural details of this interaction are unknown due to the marginal stability of the TssK-TssL complex. Here we conducted a mutagenesis study based on putative TssK-TssL contact pairs identified by co-evolution analyses. We then evaluated the impact of these mutations on T6SS activity, TssK-TssL interaction and sheath assembly and dynamics in enteroaggregative *Escherichia coli*. Finally, we probed the TssK-TssL interface by disulfide cross-linking, allowing to propose a model for the baseplate-membrane complex interface.

INTRODUCTION

The type VI secretion system (T6SS) is a molecular nanoweapon that uses a contractile mechanism to propel an effector-loaded needle into bacterial and/or eukaryotic target cells[1-4]. The T6SS is comprised of two complexes[2, 4-6]. The tail structure is constituted of the baseplate (BP) complex on which the tube-sheath complex is polymerized[7-9]. The BP complex is made of six TssEFGK wedges surrounding the VgrG spike[7-11]. The tail tube-sheath complex is composed of the inner tube, made of stacked Hcp hexamers, wrapped by the TssBC sheath[12-14]. The base of the VgrG spike serves as initiator for the polymerization of the inner tube, while the wedge complexes prime sheath polymerization[15,16]. The sheath polymerizes under an extended conformation, and contracts upon contact with the target cells or in response to other signals, propelling the tube-spike needle, loaded with effectors, into the target[6,13,17-23]. The passage of the tube-spike needle across the cell envelope of the attacker cell necessitates the membrane complex (MC), which also serves as docking station for the baseplate[8,24]. The membrane complex is composed of the TssL and TssM inner membrane proteins, and of the TssJ outer membrane lipoprotein[24-29]. Interestingly, the tail and membrane complexes present different evolutionarily histories. The TssL and TssM subunit of the MC share homologies with components of the Type IVb secretion system[30-32]. By contrast, with the exception of the TssK subunit, the tail proteins are conserved within the large family of contractile injection systems, which also include members of the Myoviridae bacteriophages and R-type pyocins[9,13,16,33-35]. The trimeric TssK wedge subunit is functionally and structurally related to receptor-binding proteins (RBP) of short non-contractile phages[36,37]. RBPs are surface proteins that recognize cell surface receptors allowing specific phage binding to target cells[38,39]. RBPs are comprised of an N-terminal shoulder domain that is anchored into the baseplate, and a C-terminal head domain that binds to specific receptors[39]. The T6SS TssK proteins has a similar organization, with an N-terminal domain anchored to the baseplate, and a C-terminal domain that binds to

the MC[7,8,36,37,40]. This interaction allows the BP to be recruited to the MC docking station but also properly positions the tail structure in order to propel the tube-spike complex across the MC channel[8,36,37]. While recent studies have provided important information on MC and BP composition and structures, molecular details on how these two T6SS complexes are connected remains incomplete. Boyer *et al*. noted that the *tssK* and *tssL* genes co-occur in most T6SS gene clusters[32], suggesting that they have coevolved to properly adapt the baseplate onto the membrane complex. Indeed, protein-protein interaction studies have shown that TssK interacts with the TssL cytoplasmic domain[8,36]. Further works demonstrated that TssK-TssL complex formation involve the TssK C-terminal head domain and the TssL L2-L3 loop[37,40]. Here, to gain further information on MC-BP contacts, we conducted a rationally-guided mutagenesis based on coevolution prediction of TssK/TssL residue pairs. The coevolution strategy proposed four sites of contacts between the two proteins that were tested by phenotypic and protein-protein interaction assays, allowing to propose a model of the MC-BP interface.

MATERIAL AND METHODS

Bacterial strains, media, chemicals and growth conditions. Strains used in this study are listed in Table S1. *E. coli* K-12 strain DH5α was used for all cloning procedures, BTH101 for bacterial two-hybrid assays, and W3110 for co-immunoprecipitation experiments. The enteroaggregative *E. coli* (EAEC) strains used in this study are all derivatives of the wild-type strain 17-2. The 17-2 *tssB-sfGFP*, Δ*tssK*, Δ*tssK tssB-sfGFP*, Δ*tssL*, and Δ*tssL tssB-sfGFP* have been previously described[8,24,26,36]. *E. coli* cells were routinely grown in Lysogeny Broth (LB) supplemented with antibiotics when necessary (kanamycin 50 µg.mL^{-1}, chloramphenicol 40 µg.mL^{-1}, ampicillin 100 µg.mL^{-1}). For T6SS expression, EAEC cells were grown in Sci1-inducing medium (SIM; M9 minimal medium supplemented with glycerol 0.25 %, vitamin B1

200 μg.mL^{-1}, casaminoacids 40 μg.mL^{-1}, $MgCl_2$ 2 mM, $CaCl_2$ 0.1 mM, and LB (10% v/v))[41]. Expression from pBAD and pTrc99A vectors was induced with L-arabinose (0.05%) and Isopropyl β-D-1-thiogalactopyranoside (IPTG, 200 μM), respectively. Dichloro (1,10-phenanthroline) copper(II) (Cu-oP) and *N*-ethylmaleimide (NEM) were purchased from Sigma-Aldrich.

Plasmid construction. Plasmids used in this study are listed in Table S1. Polymerase Chain Reactions (PCR) were performed using a Biometra thermocycler using Q5 DNA polymerase (New England Biolabs). Custom oligonucleotides, listed in Table S1, were synthesized by Sigma Aldrich. Bacterial two-hybrid vectors producing TssK or TssL fused to the *Bordetella* adenylate cyclase T18 or T25 domains, and plasmid pBAD-TssK^{V}, producing TssK fused to a C-terminal VSV-G, have been previously published[36]. Plasmid pTrc-TssLST, producing TssL fused to a C-terminal Streptag II, was constructed by restriction free (RF) cloning[42]. Briefly, the DNA fragment corresponding to the *tssL* gene was amplified using primers that introduced extensions annealing to the target vector. The double-stranded product of the first PCR has then been used as primer for a second PCR using the target vector as template. PCR products were then treated with DpnI to eliminate template plasmids and transformed into DH5α-competent cells. The pKO3-*tssL* vector was engineered by restriction/ligation cloning of a *Bam*HI-*Sal*I DNA fragment encompassing the *tssL* gene into pKO3[43]. Substitutions were introduced by site-directed mutagenesis using complementary oligonucleotides bearing the desired mutation. All plasmids have been verified by DNA sequencing (Eurofins).

Strain engineering. The Δ*tssKL* strain was constructed by the one-step inactivation procedure[44] using λ-red recombination carried by vector pKOBEG[45], and a PCR product corresponding to the pKD4 kanamycin cassette[44] flanked by 50-bp extensions annealing upstream and downstream the region to be deleted. Recombinant strains were selected on LB

plates supplemented with kanamycin, and the kanamycin cassette was excised mutations by the Flp FRT recombinase carried by vector pCP20[44]. Strains 17-2 bearing point mutations at the chromosomal *tssL* locus have been engineered using the suicide vector pKO3[43]. The first and second recombination events were selected on LB plates supplemented with chloramphenicol at 42°C, and supplemented with sucrose (5%), respectively, as previously described[43]. All strains were verified by colony-PCR using various oligonucleotide pair combinations. Strains with chromosomal point mutations were further verified by PCR amplification of the region of interest and DNA sequencing.

Protein-protein interaction assays. Bacterial two-hybrid assays were conducted as previously described[36]. Pull-down experiments were performed as previously described[40] with modifications: protein samples were subjected to pull-down on StrepTactin sepharose (Cytiva) and CellLytic B buffer (diluted 1/5, Sigma-Aldrich) was added in the washing buffer.

Disulfide bond formation assay. Disulfide bond formation assays were performed as previously published[14,15]. Briefly, cells producing the *tssK* and *tssL* cysteine derivatives were grown to an absorbance at λ=600 nm (A_{600}) of ~ 0.6 and then incubated with 0.3 mM of Cu-oP for 20 min without agitation. About 3×10^{10} cells were then harvested by centrifugation and resuspended in 0.5 mL of 10 mM HEPES (pH7.4), 30% sucrose, 1 mM EDTA and 2.5 mM NEM for 30 min on ice to block free thiol groups. Cells were pelleted by centrifugation and mixed with loading buffer prior to analysis by SDS-PAGE and immunoblotting.

Anti-bacterial assays. The antibacterial growth competition assay was performed as described[46] with modifications. The WT *E. coli* strain W3110 bearing the pUA66-*rrnB* plasmid ($Kan^{R,}$ [47]) was used as recipient in the competition assay. The pUA66-*rrnB* plasmid provides a strong constitutive green fluorescent (GFP^{+}) phenotype. Attacker and recipient cells were grown in SIM medium to an A_{600} of 0.6-0.8, harvested and normalized to a A_{600nm} of 0.6 in SIM.

Attacker and recipient cells were mixed to a 4:1 ratio and 10-µL drops of the mixture were spotted in triplicate onto a prewarmed dry SIM agar plate. After 4-hour incubation at 37°C, fluorescent images were recorded with a LI-COR Odyssey imager. The bacterial spots were scratched off, cells were resuspended in LB medium supplemented with kanamycin, normalized to an A_{600} of 0.5 and serially diluted. One hundred µL of serial dilutions were then spread in triplicate on LB plates supplemented with kanamycin to select surviving recipients. Colony forming units were numbered after overnight incubation at 37°C. The experiment was done in triplicate.

Live fluorescence microscopy. Cells were grown in SIM medium at 37°C to an A_{600} of 0.6-0.8, resuspended in fresh SIM to an $A_{600\,nm}$ of 10, and 5 µL were spotted onto a thin pad of SIM supplemented with 2% agarose covered with a glass coverslip. Phase contrast and fluorescence were recorded on a Nikon Eclipse Ti2 microscope equipped with a 100 × NA 1.45 Ph3 objective, an Orca-Fusion digital camera (Hamamatsu) and a perfect focus system. All fluorescence images were acquired with a minimal exposure time to minimize bleaching and phototoxicity effects. Exposure times were typically 30 ms for phase contrast, 100 ms for TssB-sfGFP. The experiments were performed at least in triplicate and representative results are shown. Images were analyzed using ImageJ (http://imagej.nih.gov/ij/) and the MicrobeJ v5.11y plugin (http://www.microbej.com/). Statistical dataset analyses were performed with several representative fields from at least three independent biological replicates, using Excel and the R software environment. The number of measured cells or events (n) is indicated on each figure.

Bioinformatics analyses. To predict residue pairs in contact between two protein domains, we combined the RaptorX complex contact prediction web server[48] and the GREMLIN monomer contact prediction web server[49]. We queried the sequences of the two protein domains in RaptorX, obtaining a multiple sequence alignment (MSA) of the two concatenated sequences.

175 The MSA is used as input in GREMLIN, which returns a list of coevolving residue pairs ranked
176 by their contact probability.

177 To obtain accurate interactions, we determined a contact probability threshold using the EAEC
178 T6SS wedge complex structure[10] as a benchmark in a binary classification study. First, we
179 obtained pairs of coevolving residues between TssK and TssG and between TssG and TssF.
180 The known structure of the wedge complex (PDB: 6N38) was used to calculate the distance
181 between the residues of each pair (minimum distance between all heavy atoms). The pairs of
182 residues were classified into close pairs, when the corresponding distance was below 8 Å, and
183 distant pairs, when the distance was above 8 Å. Additionally, by defining an arbitrary contact
184 probability threshold, the pairs were classified as predicted interacting pairs, when the
185 corresponding contact probability was above the threshold, and predicted non-interacting pairs,
186 contact probability below the threshold. Hence, given a contact probability threshold, close
187 pairs predicted as interacting were considered as true positives (TP), and close pairs predicted
188 as non-interacting are false negative (FN). Similarly, false positives (FP) and true negatives
189 (TN) correspond to distant pairs predicted as interacting or non-interacting, respectively.
190 Finally, we computed the precision (TP/(TP+FP)) of the binary classification for a given contact
191 probability threshold. To determine the high-confidence threshold, we maximized TPs while
192 minimizing the FPs. Setting a probability threshold of 0.9 and selecting all pairs with a
193 probability above this threshold allowed us to select no FP's (Supplementary Figure 1a) and a
194 maximal precision (Supplementary Figure 1b). Hence, we used the high-confidence threshold
195 to filter the interactions predicted for TssK-Ct, and $TssL_C$. All the data and scripts used for this
196 methods section were deposited in Git repository
197 (https://github.com/ishon92/CoevolutionTssKL.git).

198 Information-driven docking simulations were performed with the standard parameters on the
199 HADDOCK 2.4 web server[50], implemented by imposing ambiguous distance constraints based
200 on the results of disulfide cross-linking data (active residues) using GenTBL[51]. AlphaFold2
201 structural models were generated using the Colabfold server using standard parameters[52-54].

202 **Miscellaneous.** Standard methods were used for sodium dodecyl-sulfate poly-acrylamide gel
203 electrophoresis (SDS-PAGE) and protein transfer on nitrocellulose membranes. Membranes
204 were probed with Strep-Tag Classic (clone Strep-tag II, Bio-Rad), and anti-VSV-G (clone
205 P5D4, Sigma-Aldrich) monoclonal antibodies, and goat anti-mouse secondary antibodies
206 conjugated to Alkaline Phosphatase (Beckman Coulter). Alkaline phosphatase signal was
207 developed in alkaline buffer (pH 9) in the presence of 10 mM $MgCl_2$, 0.15 mg/mL of 5-bromo-
208 4-chloro-3-indolylphosphate and 0.3 mg/mL of nitroblue tetrazolium.

209

210 **RESULTS AND DISCUSSION**

211 **Co-evolution analyses propose a potential interface between the TssK C-terminal domain**
212 **and the TssL cytoplasmic domain.**

213 To better understand how the T6SS baseplate is connected to the membrane complex (Figure
214 1a), we first conducted bioinformatic analyses. Previous co-occurrence analyses have shown
215 that the *tssK* gene co-occurs with the *tssL* gene[32], and further protein-protein interaction studies
216 demonstrated that the C-terminal domain of TssK (TssK-Ct) engages interaction with the
217 cytoplasmic domain of TssL, $TssL_C$[36,37,40]. We thus predicted the residue-residue interactions
218 between TssK-Ct and $TssL_C$ by combining coevolution analysis with binary classification. First,
219 the predicted contacts were ranked based on the probability scores obtained from web servers
220 dedicated to estimating residue-residue covariation. Second, enforcing a binary classification

on the known T6SS baseplate wedge complex structure[10], four high-confidence interacting pairs were selected between TssK-Ct and $TssL_C$: TssK-Ala381/TssL-L76, TssK-Ala381/TssL-Gln94, TssK-Val390/TssL-Arg141, and TssK-Pro429/TssL-Pro92 (Table 1) (Figure 1b and 1c). Interestingly, TssK residues in the predicted pairs are located into loops that protrude on the top of the T6SS wedge structure[10], while TssL residues in these pairs are located in close proximity to a region of the TssL cytoplasmic domain previously shown to be required for TssK-L interaction[40].

Impact of TssK and TssL mutations on T6SS antibacterial activity.

We first tested the importance of the TssK and TssL potential interfacial residues for T6SS activity. The EAEC Sci1 T6SS was previously shown to confer a competitive advantage against a K-12 laboratory strain of *E. coli*, through the secretion of the Tle1 phospholipase[46]. A *E. coli* K-12 strain carrying a vector that confers constitutive GFP fluorescence and kanamycin resistance was used as recipient. The EAEC T6SS Sci1 activity was estimated by the fluorescence of the attacker/recipient mixture after 4 hours of co-incubation (Figure 2, lower panels), and quantified by counting the number of surviving recipients on selective kanamycin plates (Figure 2, upper panels). The *tssK* and *tssL* mutations were introduced on the chromosome, at the native locus. Figure 2 shows that TssK substitution A381W, and TssL substitutions L76W, Q94W and P92A abolish T6SS activity, whereas TssK substitutions V390W and P429A and TssL substitution R141D significantly decrease T6SS activity without abolishing it.

Impact of mutations on T6SS sheath assembly, dynamics and stability.

To gain further insights onto the impact of these mutation on T6SS assembly and function, we conducted fluorescence microscopy analyses, using a fusion of the superfolder-GFP (sfGFP) to

TssB, one of the T6SS sheath subunits. As previously described, about ~ 60% of wild-type EAEC TssB-sfGFP cells produce T6SS sheath structures (Figure 3a and 3b)[55]. While the majority of these cells produce a single T6SS structure, up to 4 structures can be observed per cell (Figure 3b). The *tssK* and *tssL* mutants presented different behaviors. While almost no sheath structure was observed in TssK-A381W and TssL-L76A, TssL-P92A and TssL-Q94W mutant cells, about of 20% of TssK-V390W cells assembled sheath structures, and TssK-P429A cells behave similarly to the wild-type (Figure 3a and 3b). With the exception of TssK-P429A, the impact of these mutations on T6SS sheath assembly is in agreement with the T6SS-dependent antibacterial activities of the corresponding mutant cells (Figure 2). The overall antibacterial activity of TssK-P429A mutant cells was significantly decreased (Figure 2) although they presented a wild-type phenotype in terms of number and distribution of T6SS sheath structures (Figure 3b). This difference prompted us to further study the impact of this mutation on T6SS dynamics. Time-lapse recordings showed that, contrarily to wild-type cells, TssK-P429A mutant cells presented aberrant contraction events (Figure 3c). Although no significant difference was observed in the residence time, *i.e.*, the time for which sheaths remain in the extended conformation prior to contraction (Figure 3d), a significant proportion of TssK-P429A sheath structures contracts in the opposite direction (i.e., contraction towards the distal extremity) or in both direction (bidirectional contraction) (Figure 3c and 3e). These observations suggest that the sheath structures break in the middle or at the basal extremity, reflecting defects in membrane complex/baseplate stability.

Impact of TssK and TssL mutations on TssK-TssL complex formation.

To provide information on the role of the coevolved residue pairs on MC-BP complex formation, the TssK-TssL$_C$ interaction was assayed by bacterial two-hybrid (BACTH, Figure

4a and 4b) and pull-down on StrepTactin sepharose (Figure 4c). BACTH analyses showed all the TssK mutants are still capable to form oligomers with wild-type TssK (Figure 4a). Similarly, all the mutations introduced in the cytoplasmic domain of TssL did not impact $TssL_C$ oligomer formation (Figure 4b). These results suggest that the TssK-T25 and $TssL_C$-T18 fusion variants are produced and properly folded. BACTH and pull-down analyses revealed that TssK mutation A381W and TssL mutations L76W and Q94W abolish interactions with $TssL_C$ and TssK, respectively, while TssK substitutions V390W and P429A, and TssL substitutions P92A and R141D impact the TssK-$TssL_C$ interaction without abolishing it (Figure 4a-c).

To gain detailed insights onto the TssK–TssL interface, we substituted the coevolved pair residues by cysteines. Thiol groups of cysteine side-chains form disulfide bonds if located at appropriate distances (Cα-Cα distance <7 Å) leading to covalent complex formation that can be observed by non-reducing SDS-PAGE analyses. TssK and TssL possess five native cysteine residues each, with two cysteines in the TssK C-terminal domain, and four on the TssL cytoplasmic domain. All these cysteine residues are buried into the structure and not accessible. In agreement with this observation, pilot experiments showed that no covalent TssK-TssL complex can be visualized upon addition of the oxidative agent copper(II) orthophenanthroline, suggesting that none of the native cysteines engages in disulfide bond formation (Supplementary Figure S2a). Figure 5a shows that higher-molecular-weight species (denoted with *) are observable for three of the four combinations: TssK-A381C/TssL-L76C, TssK-A381C/TssL-Q94C and TssK-P429C/TssL-P92C. The apparent molecular weight of these species (~ 68 kDa) is compatible with a complex between TssK (theoretical weight: 49 kDa) and TssL (theoretical weight: 23 kDa). These complexes are likely to be covalently bound by disulfide bridges as they dissociated upon the addition of a reducing agent (Figure 5a) and likely comprise both TssK and TssL as they are recognized by both the anti-VSV-G and -StrepTag antibodies (Figure 5b). As control experiments for specificity, we also tested all combinations

293 corresponding to non-coevolved pairs. In these conditions, no TssKL complex was observed
294 (Supplementary Figure S2b), demonstrating the specificity of disulfide bridge formation
295 between the TssK-A381C/TssL-L76C, TssK-A381C/TssL-Q94C and TssK-P429C/TssL-P92C
296 coevolved pairs, but also that none of the native cysteine residues of TssK and TssL engage
297 interaction with the substituted cysteines. A summary of the contacts is shown in Figure 5c.

298

299 **CONCLUDING REMARKS**

300 Although the biogenesis and mechanism of action of the T6SS are well described, details are
301 yet missing regarding the interaction between subcomplexes, and notably subcomplexes with
302 different evolutionarily histories. The phage related TssEFGK baseplate complex is recruited
303 to the T4bSS-like TssJLM membrane complex via interactions between the C-terminal domain
304 of TssK and the cytoplasmic domain of TssL. In this study, we used coevolution programs to
305 identify potential contact pairs between the TssK and TssL proteins, suggesting a model for the
306 interface of the heterodimer. The residues involved in the contacts were targeted by
307 mutagenesis and the impact of the corresponding mutations was assayed by interbacterial
308 competition, fluorescence microscopy and protein-protein interaction assays. These analyses
309 revealed that residues TssK A381 and TssL L76 and Q94 participate to TssK-L complex
310 formation and are hence required for efficient assembly of the T6SS. The TssK V390 and P429
311 and TssL P92 and R141 mutations caused a reduced number or aberrant behavior of T6SS
312 sheaths, which could be caused by the instability of the MC-BP complex. The results of the
313 disulfide cross-linking assays showed that TssK residue A381 and TssL residues L76 and Q94,
314 and TssK residue P429 and TssL residue P92 are at close proximity and can engage in disulfide
315 bond formation when substituted by cysteines.

316 Comparison of the protein-protein interaction and phenotypic analyses suggest that substituting
317 TssK-A381, TssL-L76 and TssL-Q94 by bulky side-chain residues has a strong impact on
318 complex formation, as well as on T6SS function, suggesting that this interface is critical for a
319 functional BP-MC interaction. By contrast, substituting TssL residue P92 did not have a
320 significant impact while substituting the coevolved partner TssK residue P429 decreased T6SS
321 function. Fluorescence microscopy recordings showed that sheaths from TssK-P429A cells are
322 less stable and can break at the base (opposite contraction) or in the middle (bidirectional
323 contraction). We suggest that the P429A mutation locally affects the TssK-Ct structure, leading
324 to the destabilization of the MC-BP interface which cannot resist the strength engendered by
325 sheath polymerization.

326 By imposing the restraints derived from the disulfide cross-linking data for the TssK-
327 A381/TssL-L76, TssK-A381/TssL-Q94, and TssK-P429/TssL-P92 residue pairs, a model of
328 the TssK-Ct-TssL$_C$ complex can be proposed (Figure 6a). Interestingly, with a root-mean-
329 square deviation (r.m.s.d) of 0.91 Å, this model is very close to the one proposed for the TssK-
330 Ct/TssL$_C$ complex by the recently released AlphaFold2 structure prediction program[52-54]
331 (Figure 6b). To completely understand the interaction between the BP and MC, some
332 unresolved issue remains to be addressed, notably how 36 TssK C-terminal domains are
333 connected to 10 TssL cytoplasmic domains. Nevertheless, this refined model of the TssK-TssL
334 interface provides detailed information on BP-MC contacts, and helps to better understand how
335 the TssK RBP-like protein has evolved to adapt to the TssL receptor in order to properly dock
336 the baseplate onto the MC.

337

338 **CRediT authorship contribution statement**

Etienne Vanlioglu: Investigation, Methodology; Writing – review & editing. Yoann G. Santin: Investigation, Methodology, Writing – review & editing. Isaac Merce-Filella: Investigation, Methodology, Writing – review & editing. Riccardo Pellarin: Conceptualization, Supervision, Investigation, Methodology, Writing – review & editing. Eric Cascales: Conceptualization, Supervision, Methodology, Funding acquisition, Writing – original draft, Writing – review & editing.

Data availability

All data are shown in the manuscript or in the supplemental material.

Declaration of competing interest

The authors declare that they have no known competing financial interests or personal relationships that could have appeared to influence the work reported in this paper.

Acknowledgements

We thank members of the Cascales laboratory and Yassine Cherrak for discussions, and Moly Ba, Isabelle Bringer, and Annick Brun for technical assistance. This work was supported by the CNRS, the Aix-Marseille Université and by grants from the Agence Nationale de la Recherche (ANR-20-CE11-0017), the Fondation pour la Recherche Médicale (DEQ20180339165) and the Fondation Bettencourt-Schueller to EC. EV was supported by the Fondation pour la Recherche Médicale.

References

1. Cianfanelli FR, Monlezun L, Coulthurst SJ. Aim, load, fire: the type VI secretion system, a bacterial nanoweapon. Trends Microbiol. 2016. 24(1):51-62. doi: 10.1016/j.tim.2015.10.005. PMID: 26549582.

2. Cherrak Y, Flaugnatti N, Durand E, Journet L, Cascales E. Structure and activity of the type VI secretion system. Microbiol Spectr. 2019. 7(4). doi: 10.1128/microbiolspec.PSIB-0031-2019. PMID: 31298206.

3. Coulthurst S. The type VI secretion system: a versatile bacterial weapon. Microbiology (Reading). 2019. 165(5):503-515. doi: 10.1099/mic.0.000789. PMID: 30893029.

4. Wang J, Brodmann M, Basler M. Assembly and subcellular localization of bacterial type VI secretion systems. Annu Rev Microbiol. 2019.S3:621-638. doi: 10.1146/annurev-micro-020518-115420. PMID: 31226022.

5. Zoued A, Brunet YR, Durand E, Aschtgen MS, Logger L, Douzi B, Journet L, Cambillau C, Cascales E. Architecture and assembly of the Type VI secretion system. Biochim Biophys Acta. 2014. 1843(8):1664-73. doi: 10.1016/j.bbamcr.2014.03.018. PMID: 24681160.

6. Basler M. Type VI secretion system: secretion by a contractile nanomachine. Philos Trans R Soc Lond B Biol Sci. 2015. 370(1679):20150021. doi: 10.1098/rstb.2015.0021. PMID: 26370934.

7. English G, Byron O, Cianfanelli FR, Prescott AR, Coulthurst SJ. Biochemical analysis of TssK, a core component of the bacterial Type VI secretion system, reveals distinct oligomeric states of TssK and identifies a TssK-TssFG subcomplex. Biochem J. 2014. 461(2):291-304. doi: 10.1042/BJ20131426. PMID: 24779861.

8. Brunet YR, Zoued A, Boyer F, Douzi B, Cascales E. The type VI secretion TssEFGK-VgrG phage-like baseplate is recruited to the TssJLM membrane complex via multiple contacts and serves as assembly platform for tail tube/sheath polymerization. PLoS Genet. 2015. 11(10):e1005545. doi: 10.1371/journal.pgen.1005545. PMID: 26460929.

9. Nazarov S, Schneider JP, Brackmann M, Goldie KN, Stahlberg H, Basler M. Cryo-EM reconstruction of type VI secretion system baseplate and sheath distal end. EMBO J. 2018. 37(4):e97103. doi: 10.15252/embj.201797103. PMID: 29255010.

10. Cherrak Y, Rapisarda C, Pellarin R, Bouvier G, Bardiaux B, Allain F, Malosse C, Rey M, Chamot-Rooke J, Cascales E, Fronzes R, Durand E. Biogenesis and structure of a type VI secretion baseplate. Nat Microbiol. 2018. 3(12):1404-1416. doi: 10.1038/s41564-018-0260-1. PMID: 30323254.

11. Park YJ, Lacourse KD, Cambillau C, DiMaio F, Mougous JD, Veesler D. Structure of the type VI secretion system TssK-TssF-TssG baseplate subcomplex revealed by cryo-electron microscopy. Nat Commun. 2018. 9(1):5385. doi: 10.1038/s41467-018-07796-5. PMID: 30568167.

12. Ballister ER, Lai AH, Zuckermann RN, Cheng Y, Mougous JD. In vitro self-assembly of tailorable nanotubes from a simple protein building block. Proc Natl Acad Sci U S A. 2008. 105(10):3733-8. doi: 10.1073/pnas.0712247105. PMID: 18310321.

13. Basler M, Pilhofer M, Henderson GP, Jensen GJ, Mekalanos JJ. Type VI secretion requires a dynamic contractile phage tail-like structure. Nature. 2012. 6;483(7388):182-6. doi: 10.1038/nature10846. PMID: 22367545.

14. Brunet YR, Hénin J, Celia H, Cascales E. Type VI secretion and bacteriophage tail tubes share a common assembly pathway. EMBO Rep. 2014. 15(3):315-21. doi: 10.1002/embr.201337936. PMID: 24488256.

15. Renault MG, Zamarreno Beas J, Douzi B, Chabalier M, Zoued A, Brunet YR, Cambillau C, Journet L, Cascales E. The gp27-like hub of VgrG serves as adaptor to promote Hcp tube assembly. J Mol Biol. 2018. 430(18 Pt B):3143-3156. doi: 10.1016/j.jmb.2018.07.018. PMID: 30031895.

16. Taylor NMI, van Raaij MJ, Leiman PG. Contractile injection systems of bacteriophages and related systems. Mol Microbiol. 2018. 108(1):6-15. doi: 10.1111/mmi.13921. PMID: 29405518.

17. Basler M, Mekalanos JJ. Type 6 secretion dynamics within and between bacterial cells. Science. 2012. 337(6096):815. doi: 10.1126/science.1222901. PMID: 22767897.

18. Basler M, Ho BT, Mekalanos JJ. Tit-for-tat: type VI secretion system counterattack during bacterial cell-cell interactions. Cell. 2013. 152(4):884-94. doi: 10.1016/j.cell.2013.01.042. PMID: 23415234.

19. Brunet YR, Espinosa L, Harchouni S, Mignot T, Cascales E. Imaging type VI secretion-mediated bacterial killing. Cell Rep. 2013. 3(1):36-41. doi: 10.1016/j.celrep.2012.11.027. PMID: 23291094.

20. LeRoux M, De Leon JA, Kuwada NJ, Russell AB, Pinto-Santini D, Hood RD, Agnello DM, Robertson SM, Wiggins PA, Mougous JD. Quantitative single-cell characterization of bacterial interactions reveals type VI secretion is a double-edged sword. Proc Natl Acad Sci U S A. 2012. 109(48):19804-9. doi: 10.1073/pnas.1213963109. PMID: 23150540.

21. Kudryashev M, Wang RY, Brackmann M, Scherer S, Maier T, Baker D, DiMaio F, Stahlberg H, Egelman EH, Basler M. Structure of the type VI secretion system contractile sheath. Cell. 2015. 160(5):952-962. doi: 10.1016/j.cell.2015.01.037. PMID: 25723169.

22. Wang J, Brackmann M, Castaño-Díez D, Kudryashev M, Goldie KN, Maier T, Stahlberg H, Basler M. Cryo-EM structure of the extended type VI secretion system sheath-tube complex. Nat Microbiol. 2017. 2(11):1507-1512. doi: 10.1038/s41564-017-0020-7. PMID: 28947741.

23. Brackmann M, Nazarov S, Wang J, Basler M. Using force to punch holes: mechanics of contractile nanomachines. Trends Cell Biol. 2017. 27(9):623-632. doi: 10.1016/j.tcb.2017.05.003. PMID: 28602424.

24. Durand E, Nguyen VS, Zoued A, Logger L, Péhau-Arnaudet G, Aschtgen MS, Spinelli S, Desmyter A, Bardiaux B, Dujeancourt A, Roussel A, Cambillau C, Cascales E, Fronzes R. Biogenesis and structure of a type VI secretion membrane core complex. Nature. 2015. 523(7562):555-60. doi: 10.1038/nature14667. PMID: 26200339.

25. Aschtgen MS, Bernard CS, De Bentzmann S, Lloubès R, Cascales E. SciN is an outer membrane lipoprotein required for type VI secretion in enteroaggregative Escherichia coli. J Bacteriol. 2008. 190(22):7523-31. doi: 10.1128/JB.00945-08. PMID: 18805985.

26. Aschtgen MS, Gavioli M, Dessen A, Lloubès R, Cascales E. The SciZ protein anchors the enteroaggregative Escherichia coli Type VI secretion system to the cell wall. Mol Microbiol. 2010. 75(4):886-99. doi: 10.1111/j.1365-2958.2009.07028.x. PMID: 20487285.

27. Felisberto-Rodrigues C, Durand E, Aschtgen MS, Blangy S, Ortiz-Lombardia M, Douzi B, Cambillau C, Cascales E. Towards a structural comprehension of bacterial type VI secretion systems: characterization of the TssJ-TssM complex of an Escherichia coli pathovar. PLoS Pathog. 2011. 7(11):e1002386. doi: 10.1371/journal.ppat.1002386. PMID: 22102820.

28. Logger L, Aschtgen MS, Guérin M, Cascales E, Durand E. Molecular dissection of the interface between the type VI secretion TssM cytoplasmic domain and the TssG baseplate component. J Mol Biol. 2016. 428(22):4424-4437. doi: 10.1016/j.jmb.2016.08.032. PMID: 27600411.

29. Rapisarda C, Cherrak Y, Kooger R, Schmidt V, Pellarin R, Logger L, Cascales E, Pilhofer M, Durand E, Fronzes R. *In situ* and high-resolution cryo-EM structure of a bacterial type VI secretion system membrane complex. EMBO J. 2019. 38(10):e100886. doi: 10.15252/embj.2018100886. PMID: 30877094.

30. Bingle LE, Bailey CM, Pallen MJ. Type VI secretion: a beginner's guide. Curr Opin Microbiol. 2008. 11(1):3-8. doi: 10.1016/j.mib.2008.01.006. PMID: 18289922.

31. Cascales E. The type VI secretion toolkit. EMBO Rep. 2008. 9(8):735-41. doi: 10.1038/embor.2008.131. PMID: 18617888.

32. Boyer F, Fichant G, Berthod J, Vandenbrouck Y, Attree I. Dissecting the bacterial type VI secretion system by a genome wide in silico analysis: what can be learned from available microbial genomic resources? BMC Genomics. 2009. 10:104. doi: 10.1186/1471-2164-10-104. PMID: 19284603.

454 33. Bönemann G, Pietrosiuk A, Mogk A. Tubules and donuts: a type VI secretion story. Mol Microbiol.
455 2010. 76(4):815-21. doi: 10.1111/j.1365-2958.2010.07171.x. PMID: 20444095.

456 34. Taylor NM, Prokhorov NS, Guerrero-Ferreira RC, Shneider MM, Browning C, Goldie KN,
457 Stahlberg H, Leiman PG. Structure of the T4 baseplate and its function in triggering sheath
458 contraction. Nature. 2016. 533(7603):346-52. doi: 10.1038/nature17971. PMID: 27193680.

459 35. Cascales E. Microbiology: And Amoebophilus invented the machine gun! Curr Biol. 2017.
460 27(21):R1170-R1173. doi: 10.1016/j.cub.2017.09.025. PMID: 29112872.

461 36. Zoued A, Durand E, Bebeacua C, Brunet YR, Douzi B, Cambillau C, Cascales E, Journet L. TssK
462 is a trimeric cytoplasmic protein interacting with components of both phage-like and membrane
463 anchoring complexes of the type VI secretion system. J Biol Chem. 2013. 288(38):27031-27041. doi:
464 10.1074/jbc.M113.499772. PMID: 23921384.

465 37. Nguyen VS, Logger L, Spinelli S, Legrand P, Huyen Pham TT, Nhung Trinh TT, Cherrak Y, Zoued
466 A, Desmyter A, Durand E, Roussel A, Kellenberger C, Cascales E, Cambillau C. Type VI secretion
467 TssK baseplate protein exhibits structural similarity with phage receptor-binding proteins and
468 evolved to bind the membrane complex. Nat Microbiol. 2017. 2:17103. doi:
469 10.1038/nmicrobiol.2017.103. PMID: 28650463.

470 38. Casjens SR, Molineux IJ. Short noncontractile tail machines: adsorption and DNA delivery by
471 podoviruses. Adv Exp Med Biol. 2012. 726:143-79. doi: 10.1007/978-1-4614-0980-9_7. PMID:
472 22297513.

473 39. Spinelli S, Veesler D, Bebeacua C, Cambillau C. Structures and host-adhesion mechanisms of
474 lactococcal siphophages. Front Microbiol. 2014. 5:3. doi: 10.3389/fmicb.2014.00003. PMID:
475 24474948.

476 40. Zoued A, Cassaro CJ, Durand E, Douzi B, España AP, Cambillau C, Journet L, Cascales E.
477 Structure-function analysis of the TssL cytoplasmic domain reveals a new interaction between the
478 Type VI secretion baseplate and membrane complexes. J Mol Biol. 2016. 428(22):4413-4423. doi:
479 10.1016/j.jmb.2016.08.030. PMID: 27600409.

480 41. Brunet YR, Bernard CS, Gavioli M, Lloubès R, Cascales E. An epigenetic switch involving
481 overlapping fur and DNA methylation optimizes expression of a type VI secretion gene cluster. PLoS
482 Genet. 2011. 7(7):e1002205. doi: 10.1371/journal.pgen.1002205. PMID: 21829382.

483 42. van den Ent F, Löwe J. RF cloning: a restriction-free method for inserting target genes into plasmids.
484 J Biochem Biophys Methods. 2006. 67(1):67-74. doi: 10.1016/j.jbbm.2005.12.008. PMID:
485 16480772.

486 43. Link AJ, Phillips D, Church GM. Methods for generating precise deletions and insertions in the
487 genome of wild-type Escherichia coli: application to open reading frame characterization. J Bacteriol.
488 1997. 179(20):6228-37. doi: 10.1128/jb.179.20.6228-6237.1997. PMID: 9335267.

489 44. Datsenko KA, Wanner BL. One-step inactivation of chromosomal genes in Escherichia coli K-12
490 using PCR products. Proc Natl Acad Sci U S A. 2000. 97(12):6640-5. doi: 10.1073/pnas.120163297.
491 PMID: 10829079.

492 45. Chaveroche MK, Ghigo JM, d'Enfert C. A rapid method for efficient gene replacement in the
493 filamentous fungus Aspergillus nidulans. Nucleic Acids Res. 2000. 28(22):E97. doi:
494 10.1093/nar/28.22.e97. PMID: 11071951.

495 46. Flaugnatti N, Le TT, Canaan S, Aschtgen MS, Nguyen VS, Blangy S, Kellenberger C, Roussel A,
496 Cambillau C, Cascales E, Journet L. A phospholipase A1 antibacterial Type VI secretion effector
497 interacts directly with the C-terminal domain of the VgrG spike protein for delivery. Mol Microbiol.
498 2016. 99(6):1099-118. doi: 10.1111/mmi.13292. PMID: 26714038.

499 47. Zaslaver A, Bren A, Ronen M, Itzkovitz S, Kikoin I, Shavit S, Liebermeister W, Surette MG, Alon
500 U. A comprehensive library of fluorescent transcriptional reporters for Escherichia coli. Nat Methods.
501 2006. 3(8):623-8. doi: 10.1038/nmeth895. PMID: 16862137.

48. Zeng H, Wang S, Zhou T, Zhao F, Li X, Wu Q, Xu J. ComplexContact: a web server for inter-protein contact prediction using deep learning. Nucleic Acids Res. 2018. 46(W1):W432-W437. doi: 10.1093/nar/gky420. PMID: 29790960.

49. Kamisetty H, Ovchinnikov S, Baker D. Assessing the utility of coevolution-based residue-residue contact predictions in a sequence- and structure-rich era. Proc Natl Acad Sci U S A. 2013. 110(39):15674-9. doi: 10.1073/pnas.1314045110. PMID: 24009338.

50. de Vries SJ, van Dijk M, Bonvin AM. The HADDOCK web server for data-driven biomolecular docking. Nat Protoc. 2010. 5(5):883-97. doi: 10.1038/nprot.2010.32. PMID: 20431534.

51. Bonvin AMJJ, Karaca E, Kastritis PL, Rodrigues JPGLM. Defining distance restraints in HADDOCK. Nat Protoc. 2018. 13(7):1503. doi: 10.1038/s41596-018-0017-6. PMID: 29942005.

52. Jumper J, Evans R, Pritzel A, Green T, Figurnov M, Ronneberger O, Tunyasuvunakool K, Bates R, Žídek A, Potapenko A, Bridgland A, Meyer C, Kohl SAA, Ballard AJ, Cowie A, Romera-Paredes B, Nikolov S, Jain R, Adler J, Back T, Petersen S, Reiman D, Clancy E, Zielinski M, Steinegger M, Pacholska M, Berghammer T, Bodenstein S, Silver D, Vinyals O, Senior AW, Kavukcuoglu K, Kohli P, Hassabis D. Highly accurate protein structure prediction with AlphaFold. Nature. 2021. 596(7873):583-589. doi: 10.1038/s41586-021-03819-2. Epub 2021 Jul 15. PMID: 34265844.

53. Mirdita M, Schütze K, Moriwaki Y, Heo L, Ovchinnikov S, Steinegger M. ColabFold: making protein folding accessible to all. Nat Methods. 2022. 19(6):679-682. doi: 10.1038/s41592-022-01488-1. PMID: 35637307.

54. Jumper J, Hassabis D. Protein structure predictions to atomic accuracy with AlphaFold. Nat Methods. 2022.19(1):11-12. doi: 10.1038/s41592-021-01362-6. PMID: 35017726.

55. Santin YG, Doan T, Lebrun R, Espinosa L, Journet L, Cascales E. In vivo TssA proximity labelling during type VI secretion biogenesis reveals TagA as a protein that stops and holds the sheath. Nat Microbiol. 2018. 3(11):1304-1313. doi: 10.1038/s41564-018-0234-3. PMID: 30275513.

56. Durand E, Zoued A, Spinelli S, Watson PJ, Aschtgen MS, Journet L, Cambillau C, Cascales E. Structural characterization and oligomerization of the TssL protein, a component shared by bacterial type VI and type IVb secretion systems. J Biol Chem. 2012. 287(17):14157-68. doi: 10.1074/jbc.M111.338731. PMID: 22371492.

LEGEND TO FIGURES

Figure 1. Schematic representation of the type VI secretion system and positions of the co-evolved residues in the TssL and TssK structures. (a) Schematic organization of the type VI secretion system representing the different subcomplexes (pink/purple, membrane complex; blue, baseplate; green, tail tube/sheath complex). IM, inner membrane; OM, outer membrane. (b) Structures of the enteroaggregative *E. coli* TssL cytoplasmic domain (orange, PDB: 3U66[56]) and TssK trimer (grey/blue, adapted from PDB: 5M30[37]). The C-terminal domain of one monomer of TssK is indicated (TssK-Ct). (c) Magnification of the TssL cytoplasmic (orange) and TssK C-terminal (blue) domains highlighting the positions of the residues identified by co-evolution analyses and targeted in this study (TssL: residues L76, P92, Q94 and R141, red spheres; TssK: residues A381, V390 and P429, orange spheres).

Figure 2. Impact of co-evolved residue substitutions on T6SS antibacterial activity. *E. coli* K-12 competitor cells (W3110 gfp^+, kan^R) were mixed with the indicated attacker cells, spotted onto SIM agar plates and incubated for 4 h at 37 °C. The fluorescence of the bacterial spots are shown and the numbers of surviving *E. coli* competitor cells (counted on selective kanamycin medium) are indicated in the upper graph (c.f.u., colony-forming unit) as boxplots/scatterplots. The dots indicate the twelve values from three independent assays. The bold horizontal bar indicates the median value, the lower and upper boundaries of the internal box plot indicate the 25th and 75th percentiles, respectively, and the whiskers indicate the 10th and 90th percentiles. Statistical significance relative to the WT strain is indicated above the plots (***, $p < 0.001$; one-tailed Wilcoxon's *t*-test).

Figure 3. Impact of co-evolved residue substitutions on T6SS sheath assembly and dynamics. (a) Representative fields of fluorescence microscopy recording of the indicated

wild-type (WT) and mutant EAEC cells producing TssB-sfGFP. Scale bar (lower right panel), 2 μm. (b) Number of TssB-sfGFP sheaths per cell. The percentage of cells with 0, 1, 2 or >2 sheaths per cell (from dark to light blue) is shown as well as standard deviations from three biological replicates. The number of analyzed cells (*n*, total number of analyzed cells from three biological replicates) is indicated on top of each bar. (c) Violin plot representation of the sheath residence time in WT (red) and TssK P429A mutant (green) cells (bold vertical bar, median values; closed red circles, mean; lower and upper boundaries of the internal box plot, 25th and 75th percentiles, respectively; whiskers, 10th and 90th percentiles; outliers, black circles). The number of analyzed sheath assembly/contraction events (*n*) is indicated on the right. The mean and s.d. are indicated on top of each violin plot. Statistical significance relative between WT and TssK-P429A cells is indicated on the right (*, $p < 0.05$; two-tailed Wilcoxon's *t*-test; *p*-value: 0.029). (d) Fluorescence microscopy time-lapse recordings of EAEC TssK P429A cells producing TssB-sfGFP (the time from the initial image is indicated on each panel) highlighting opposite contraction (contraction towards the distal extremity of the sheath reflecting break at the basal extremity, yellow arrows) and bidirectional contraction (contraction towards both extremities reflecting break in the center of the sheath, blue arrows). The quantitative analyses (canonical, opposite and bidirectional contractions in blue, dark green and light green, respectively) are shown in panel (e), as well as standard deviations from three biological replicates. The number of sheath events analyzed for each strain (*n*, total number of analyzed cells from three biological replicates) is indicated on top of each bar.

Figure 4. Impact of co-evolved residue substitutions on TssK-TssL interaction. (a and b) Bacterial two-hybrid analysis. BTH101 reporter cells producing the indicated domains/proteins and variants (a, TssK variants; b, TssL variants) fused to the T18 and T25 domain of the *Bordetella* adenylate cyclase were spotted on X-Gal-IPTG reporter LB agar plates. The blue color of the colony reports interaction between the two partners. Controls include T18 and T25

fusions to Pal and TolB, two proteins that interact but unrelated to the T6SS. (c) Pull-down assay. Soluble lysates of *E. coli* cells producing the wild-type (WT) or variant VSV-G-tagged TssK ($TssK^{V}$) and Strep-tagged TssL ($TssL^{ST}$) proteins were subjected to pull-down on StrepTactin beads. The total lysates (T) and pulled-down material (P) were separated by 12.5%-acrylamide SDS-PAGE and immunodetected with anti-VSV-G (upper panel) and anti-StrepTag II (lower panel) monoclonal antibodies. The positions of $TssK^{V}$ and $TssL^{ST}$ are indicated on the right. Note that TssK migrates as a doublet, as previously observed[36,40]. Molecular weight markers (in kDa) are indicated on the left.

Figure 5. Disulfide cross-linking identifies TssK-TssL contacts. (a and b) Cells producing the indicated VSV-G-tagged TssK ($TssK^{V}$) and Strep-tagged TssL ($TssL^{ST}$) cysteine variants were subjected to *in vivo* oxidative treatment with copper-orthophenanthroline. After quenching with *N*-ethyl maleimide, total cell extracts were subjected to 11%-acrylamide SDS-PAGE and immunodetected with the anti-VSV-G (upper panel in panel a; "V" panels in panel b) and anti-StrepTagII (lower panel in panel a; "ST" panels in panel b) monoclonal antibodies. In panel a, samples were treated (+) or not (−) with β-mercaptoethanol. In panel b, each lane was cut vertically in two halves after protein transfer on nitrocellulose membrane (white lines) and each half was immuno-detected with the anti-VSV-G (V) or anti-StrepTagII (ST) antibody. The positions of $TssK^{V}$, $TssL^{ST}$ and of the $TssK^{V}$-$TssL^{ST}$ complex (*) are indicated on the right. Molecular weight markers (in kDa) are indicated on the left. (c) Summary of the contacts (bold lines) identified by disulfide cross-linking between the TssK (blue) and TssL (orange) cysteine variants. The co-evolved residue pairs are indicated by the colored shades (TssK-P429/TssL-P92, green; TssK-A381/TssL-L76 and TssL-A381/TssL-Q94, cyan; TssK-V390/TssL-R141, pink).

Figure 6. Model of the EAEC TssK–TssL$_C$ complex. (a) Disulfide cross-linking constrained model of the TssK-Ct (blue) / TssL$_C$ (orange) complex. The co-evolved residue pairs engaged in disulfide cross-linking are shown in green and cyan (TssK-P429/TssL-P92, green; TssK-A381/TssL-L76 and TssL-A381/TssL-Q94, cyan) while the pair that does not form disulfide bond (TssK-V390/TssL-R141) is shown in pink. (b) Overlayed comparison of the experimental-based constrained model (same color as in panel a) with the model generated by the AlphaFold2 prediction program (grey).

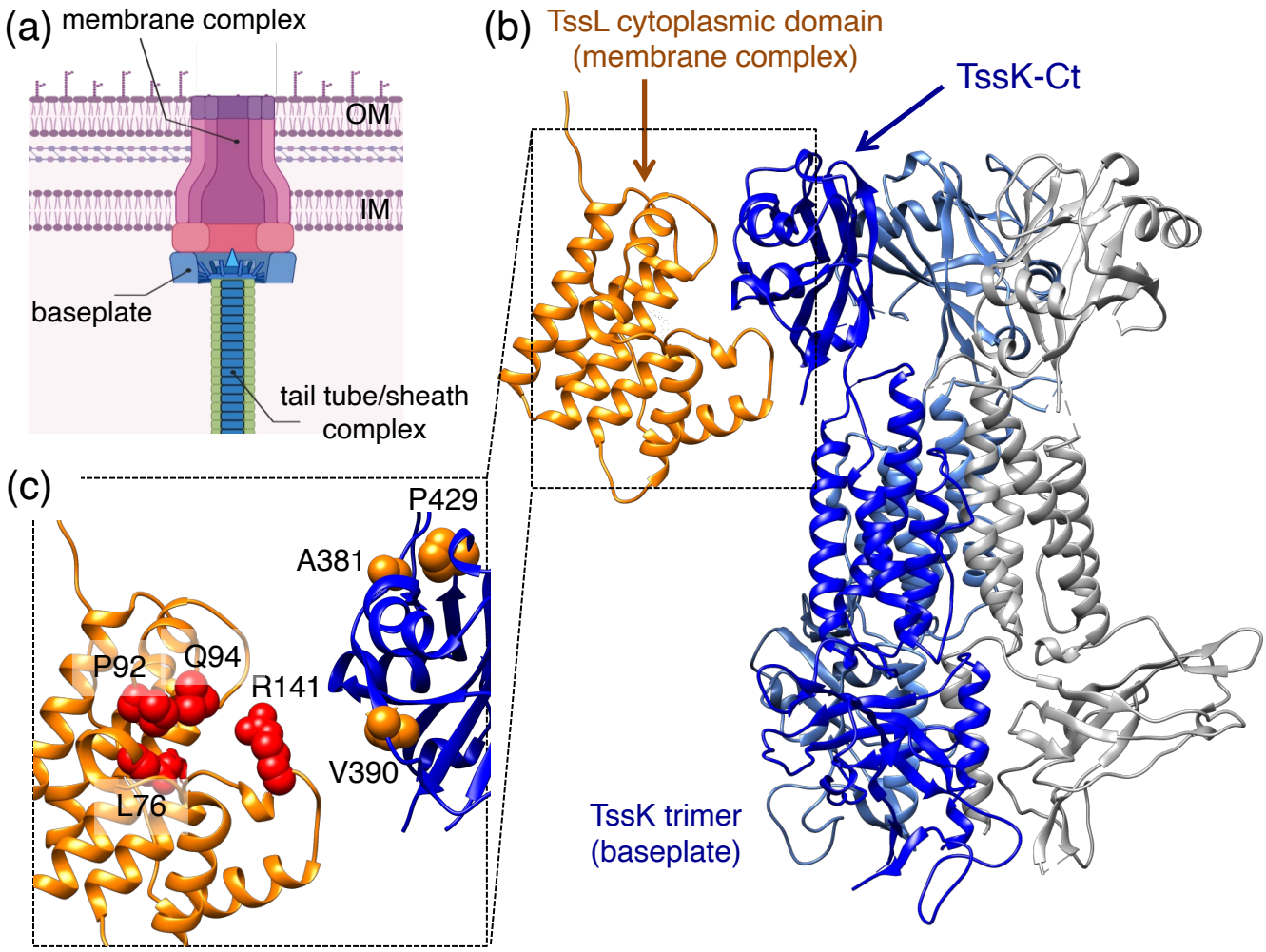
(a)
membrane complex
OM
IM
baseplate
tail tube/sheath
complex
(b)
TssL cytoplasmic domain
(membrane complex)
TssK-Ct
TssK trimer
(baseplate)
(c)
P429
A381
P92
Q94
R141
V390
L76

Figure 1

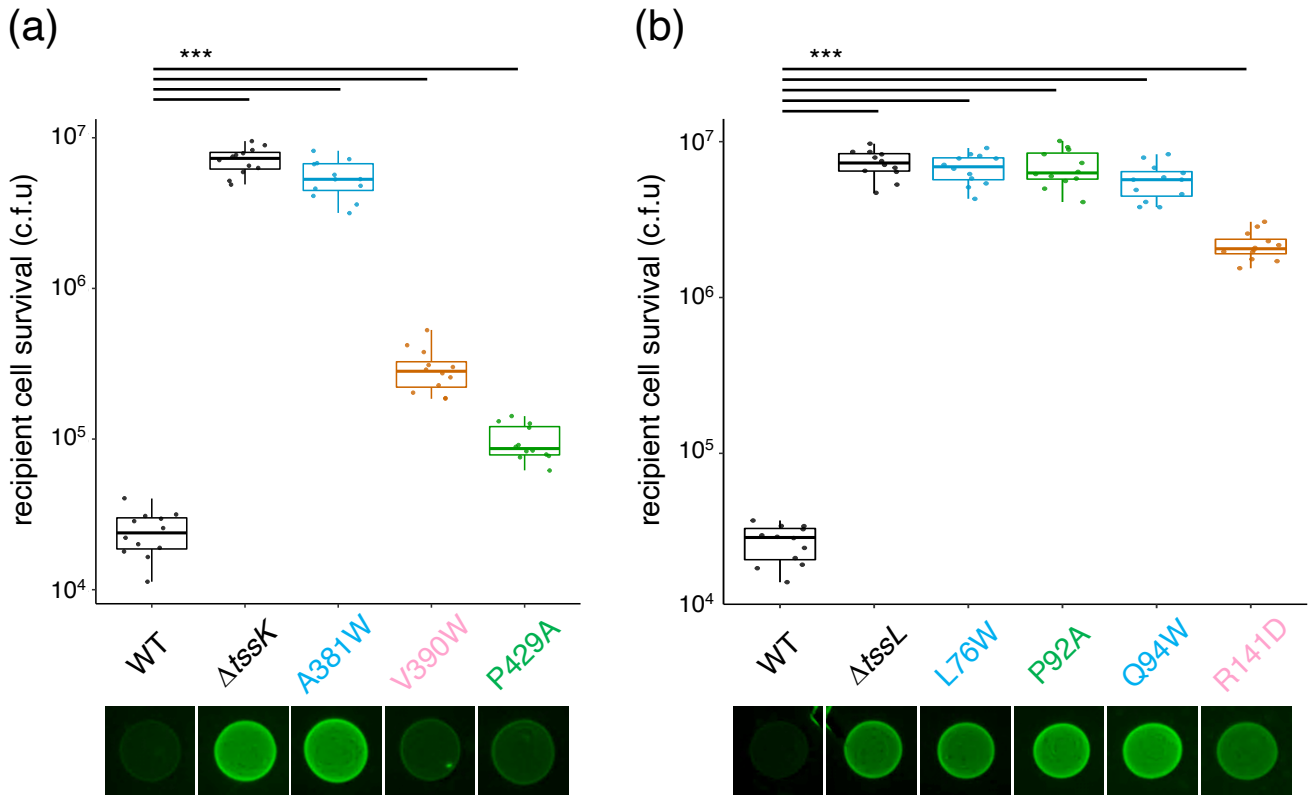
(a)
***
recipient cell survival (c.f.u)
10^7
10^6
10^5
10^4
WT
ΔtssK
A381W
V390W
P429A
(b)
***
recipient cell survival (c.f.u)
10^7
10^6
10^5
10^4
WT
ΔtssL
L76W
P92A
Q94W
R141D

Figure 2

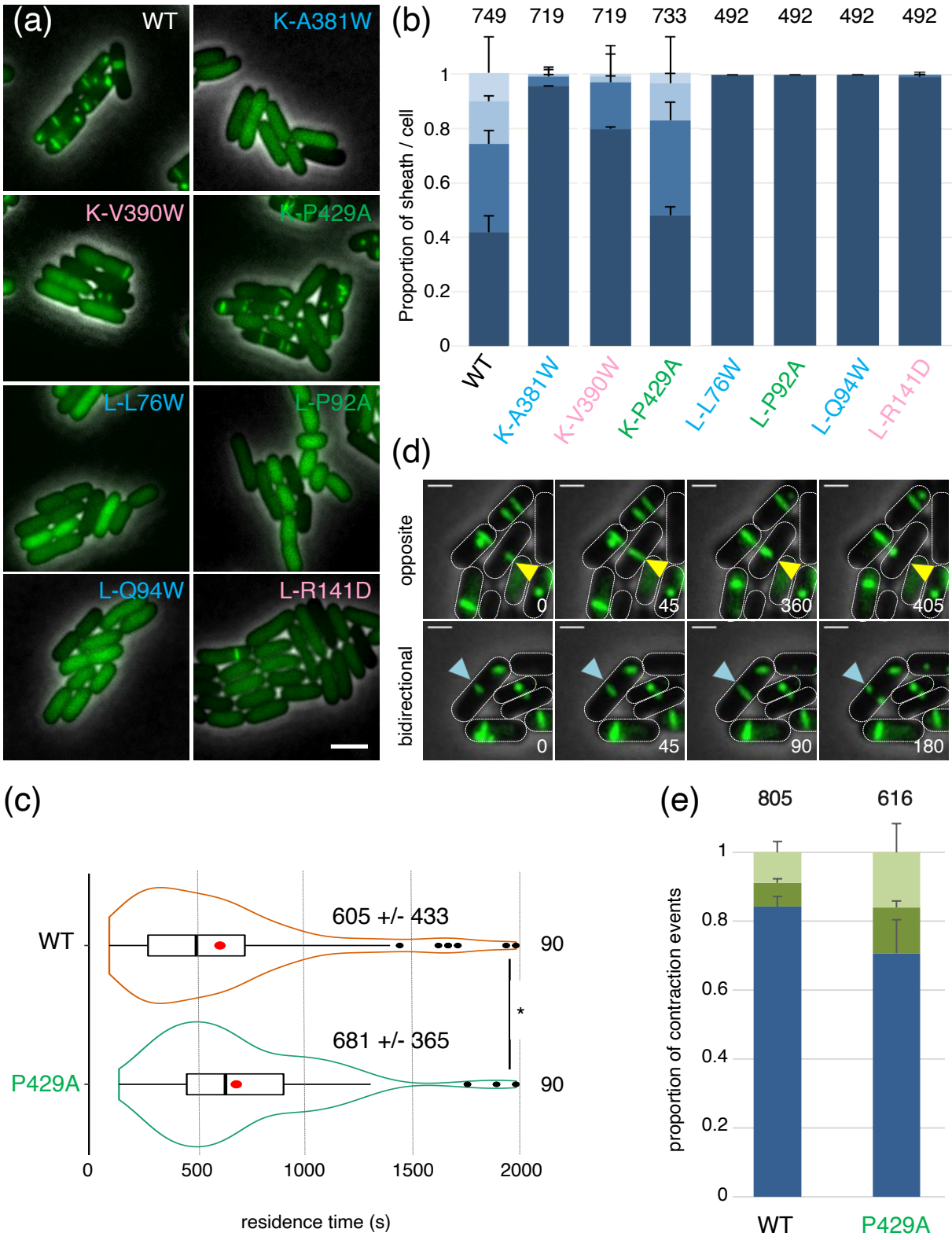
(a)
WT
K-A381W
K-V390W
K-P429A
L-L76W
L-P92A
L-Q94W
L-R141D
(b)
749 719 719 733 492 492 492 492
Proportion of sheath / cell
1
0.8
0.6
0.4
0.2
0
WT
K-A381W
K-V390W
K-P429A
L-L76W
L-P92A
L-Q94W
L-R141D
(d)
opposite
0
45
360
405
bidirectional
0
45
90
180
(c)
WT
605 +/- 433
90
*
P429A
681 +/- 365
90
0
500
1000
1500
2000
residence time (s)
(e)
805 616
proportion of contraction events
1
0.8
0.6
0.4
0.2
0
WT
P429A

Figure 3

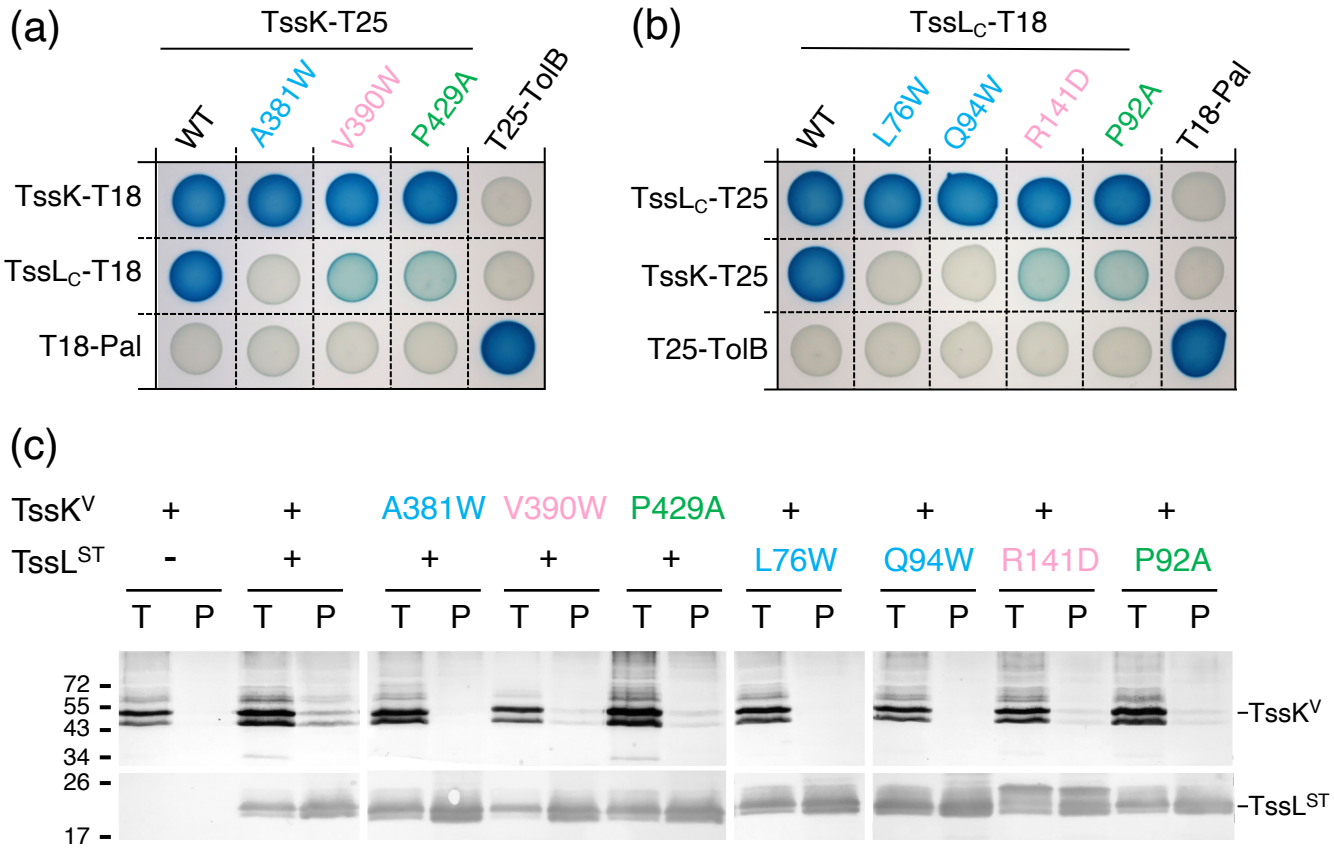
(a)
TssK-T25
WT
A381W
V390W
P429A
T25-TolB
TssK-T18
TssL$_C$-T18
T18-Pal
(b)
TssL$_C$-T18
WT
L76W
Q94W
R141D
P92A
T18-Pal
TssL$_C$-T25
TssK-T25
T25-TolB
(c)
TssK^V
TssLST
A381W
V390W
P429A
L76W
Q94W
R141D
P92A
T P
72
55
43
34
26
17
-TssK^V
-TssLST

Figure 4

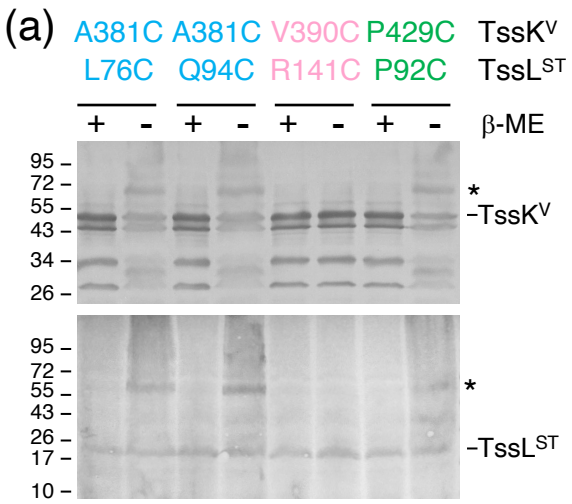
(a)
A381C L76C
A381C Q94C
V390C R141C
P429C P92C
TssK^V
TssL^ST
+ - + - + - + -
β-ME
95
72
55
43
34
26
*
-TssK^V
95
72
55
43
26
17
10
*
-TssL^ST

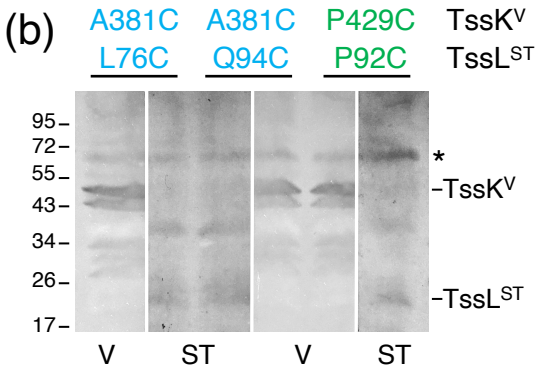
(b)
A381C L76C
A381C Q94C
P429C P92C
TssK^V
TssL^ST
95
72
55
43
34
26
17
*
-TssK^V
-TssL^ST
V
ST
V
ST

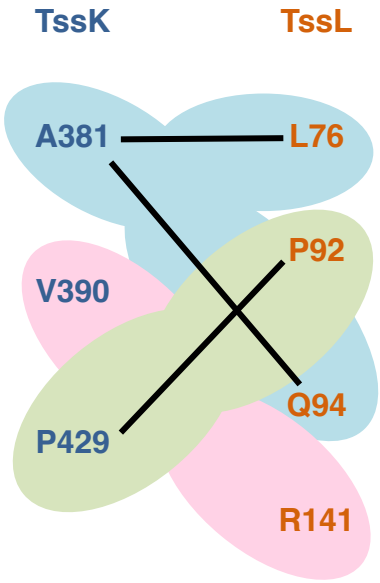
(c)
TssK
TssL
A381
L76
P92
V390
Q94
P429
R141

Figure 5

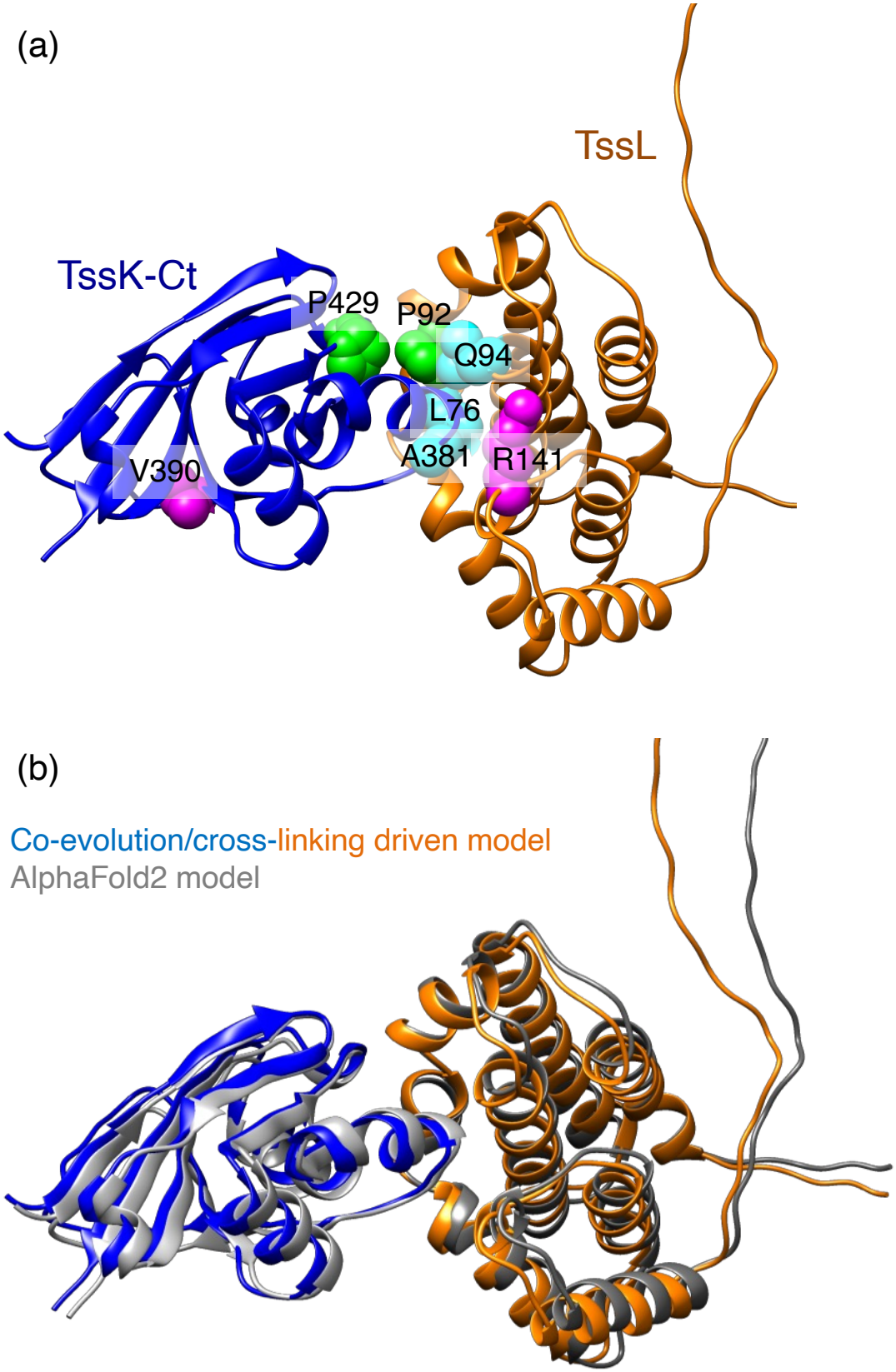
(a)
TssL
TssK-Ct
P429
P92
Q94
L76
A381
R141
V390
(b)
Co-evolution/cross-linking driven model
AlphaFold2 model

Figure 6